Galaxy Clusters from the DESI Legacy Imaging Surveys. II. Environment effects on size-mass relation

Zhaobin Chen,[1] Yizhou Gu,[2] Hu Zou,[3] and Qirong Yuan[1]

[1]*School of Physics and Technology, Nanjing Normal University, No. 1, Wenyuan Road, Nanjing, 210023, P. R. China;*
yuanqirong@njnu.edu.cn
[2]*Department of Astronomy, School of Physics and Astronomy, and Shanghai Key Laboratory for Particle Physics and Cosmology,*
Shanghai Jiao Tong University, Shanghai 200240, P. R. China
[3]*Key Laboratory of Optical Astronomy, National Astronomical Observatories, Chinese Academy of Sciences, Beijing 100012, P. R. China*

ABSTRACT

To investigate the environment effects on size growth of galaxies, we study the size-mass relation across a broad range of environment with a vast sample of approximately 32 million galaxies at $z < 0.5$ from the DESI Legacy Imaging Surveys. This sample is divided into 3 subsamples representing galaxies within three different environments: brightest cluster galaxies (BCGs), other cluster galaxies, and field galaxies. The BCGs in our large sample are dominated by quiescent galaxies (QGs), while only a minority ($\sim$13%) of BCGs are star-forming galaxies (SFGs). To demonstrate the influence of environment on size growth, we attempt to observe the difference in size-mass relation for these three subsamples. In general, the slope differences between QGs and SFGs within various environments are significant, and tend to be greater at higher redshifts. For the mass-complete subsamples at $z < 0.5$, BCGs are found to have the highest slope of size-mass relation, and no difference in size-mass relation is found between cluster members and field galaxies. To assess whether the observed slope differences stem from the variations in environment or mass distribution, we construct the mass-matched subsamples for QGs and SFGs. As a result, both QGs and SFGs show negligible difference in slope of size-mass relation among the galaxies within three distinct environments, indicating that stellar mass is the most fundamental factor driving the size evolution at $z < 0.5$, though the mass growth mode for QGs and SFGs may have been affected by galaxy environment.

Keywords: Galaxy evolution (594); Galaxy environments (2029); Brightest cluster galaxies (181)

1. INTRODUCTION

In the standard hierarchical model, weak density perturbations in the early Universe lead to the gradual collapse of dissipationless dark matter into dense dark matter halos (Mo et al. 1998). Within these halos, primitive gas gradually cools to form gaseous nebulae, which, under the influence of gravitational potential wells, collapse into dense, luminous nuclei, or galaxies (e.g., White & Rees 1978; White & Frenk 1991). As galaxies evolve, collisions and mergers occur, resulting in the formation of larger galaxies. Throughout this process, the angular momentum provided by dark matter halos dominates the size of galaxies (e.g., Mo et al. 1998; Kravtsov 2013; Huang et al. 2017). Thus, tracking the coevolution of

Corresponding author: Qirong Yuan
yuanqirong@njnu.edu.cn

galaxy size and mass with cosmic time provides insight into the assembly history of galaxies.

Stellar mass, as an important factor in the growth of galaxy size, has been extensively studied (e.g., Shen et al. 2003; Williams et al. 2010; Shibuya et al. 2015). Stellar mass assembly is a crucial process in galaxy evolution, which is influenced by intricate factors, such as star formation and mergers (e.g., Ilbert et al. 2010; Webb et al. 2015; van Dokkum et al. 2010). Usually, massive galaxies form earlier than lower-mass galaxies (e.g., Gu et al. 2018; Khullar et al. 2022), although some studies on individual galaxies suggest somewhat different histories of stellar mass assembly (e.g., Webb et al. 2022). According to Bluck et al. (2012), mergers are considered as the predominant factor driving the observed size evolution in massive galaxies below $z \sim 3$, resulting in a threefold increase in mass from $z = 3$ to the present day solely through merging. Numerous

investigations suggest that minor mergers may have a noteworthy impact on the growth of quiescent galaxies (e.g., Naab et al. 2007; Newman et al. 2012; Greene et al. 2012; van Dokkum et al. 2015; Whitney et al. 2019). In addition, McLure et al. (2013) reports compelling evidence supporting the notion that minor mergers play a crucial role in the evolution of massive galaxies at $1.3 < z < 1.5$. van Dokkum et al. (2010) found that the mass in the central regions of massive galaxies remains roughly constant with redshift, and their growth since $z \sim 2$ is only due to the gradual increase in their outer envelopes.

Williams et al. (2009) suggest that the bimodal distribution of galaxies in color space can be traced back to $z \sim 2$. In general, star-forming galaxies (SFGs) with a bluer color, whose mass growth is dominated by star formation, become quiescent galaxies (QGs) with a redder color after quenching (e.g., Schawinski et al. 2014; Bait et al. 2017; Gu et al. 2019). It is widely believed that the star formation activity in galaxies is closely related to their morphologies (Calvi et al. 2018; Nersesian et al. 2019). Morphologically speaking, SFGs with disc-dominated morphologies, which are inclined to late-type galaxies, are considered to be growing inside-out through continuous star formation (e.g., Pichon et al. 2011; Bird et al. 2013). However, QGs are inclined to early-type galaxies with elliptical or bulge-dominated morphologies. According to the work of Paspaliaris et al. (2023), only 8% of late-type galaxies are quiescent.

The correlation between galaxy morphology and environmental density has long been established (e.g., Oemler 1974; Dressler 1980). The divergence in the environmental distribution of blue and red galaxies appears since $z < 1.5$ (Gu et al. 2018). Field and cluster galaxies represent two distinct populations residing in markedly different environments, and extensive research has been conducted to explore the processes of star formation and mass assembly within each of these populations (e.g., Bundy et al. 2006; Kim et al. 2023). From a theoretical perspective, cluster galaxies in denser environment are suffering more effects of the dense and hot intracluster medium than field galaxies (e,g, Gunn & Gott 1972; Bekki & Couch 2003). Indeed, Yoon et al. (2017) find that local early-type galaxies in the densest environment with stellar mass greater than $10^{11.2} M_\odot$ tend to have larger sizes than those in low-density environment. While some researchers have suggested that cluster galaxies may be slightly smaller when compared to their counterparts in the field (e.g., Poggianti et al. 2013; Cebrián & Trujillo 2014). Despite the different conclusions reached by these studies, they all share the common idea that galaxy morphology is closely related to the environment. Nevertheless, Saracco et al. (2017) demonstrate that at approximately $z = 1.3$, the structures and intrinsic properties (namely, the equivalent median effective radius and radius normalized mass) of cluster and field elliptical galaxies are comparable. Similarly, Weinmann et al. (2009) find that no differences in radius are observed between early-type central and satellite galaxies. The analysis of Huertas-Company et al. (2013a) also indicates no significant environmental dependence for the sizes of central and satellite early-type galaxies at fixed stellar mass at $z \sim 0$.

Among the member galaxies of cluster, the brightest cluster galaxies (BCGs) are expected to have a more complex evolution process, due to the association with dense environment at the center of cluster. Generally, BCGs are found close to the center of galaxy clusters with the densest environment, which has been determined by X-ray or gravitational lens observations (e.g., Jones & Forman 1984; Smith et al. 2005). Compared with member and field galaxies, BCGs may have a more complex pattern of mass growth (e.g., Kluge et al. 2020). Simulations and semi-analytic models show that BCGs assemble most of their stellar mass through multiple mergers (e.g., Dubinski 1998; De Lucia & Blaizot 2007). Observational studies also suggest that merger plays an important role in the evolution of BCGs (e.g., Lidman et al. 2013; Lavoie et al. 2016). Further investigations on the stellar mass evolution of BCGs show that their mass increases as redshift decreases (e.g., Lidman et al. 2012), while others maintain that the stellar mass has remained constant since at least $z \sim 1$ (e.g., Whiley et al. 2008; Ascaso et al. 2011). The work of Webb et al. (2015) demonstrates that the evolutionary pattern of stellar mass varies with redshift. Specifically, when redshifts exceed 1, the dominant force driving the growth of stellar mass may be the process of star formation, whereas at lower redshifts ($z < 1$), dry mergers are likely to play a more significant role in this phenomenon. Some studies suggest that the growth rate of BCG mass may exhibit a slowdown, with more rapid growth observed at $z > 0.5$ and slower growth at $z < 0.5$ (e.g., Lin et al. 2013; Oliva-Altamirano et al. 2014). In addition, diverse perspectives in research provide unique insights, such as the study by Ascaso et al. (2011) on the evolution of BCGs over the past approximately 6 Gyr. They believe that the only mechanism that is able to explain the evolution in BCG size and the non-evolution in the BCG Sérsic shape parameter during the last 6 Gyrs are the feedback processes (such as galactic winds and ejection).

Taking into account the environment as a variable in our study, we attempt to investigate whether it plays a

significant role in the variation of the size-mass relation ($R_{\rm e} \propto M_*^\alpha$). In this paper, we select three subsamples for our analysis, including field galaxies, member galaxies, and BCGs. Based on the ninth publicly released data of the Dark Energy Spectroscopic Instrument (DESI) Legacy Imaging Surveys, we can obtian more than 32 million galaxies with a sky area of $\sim 20{,}000$ deg^2 in the redshift range of $0 < z < 0.5$. The influence of environment on size-mass relation is analyzed. This paper is the second in our series of works (the first study has already been completed by Zou et al. 2021) and is organized as follows. In Section 2, we describe the catalogue of data from the DESI Legacy Imaging Surveys and the detailed process to construct samples. In Section 3, we analyze the detailed influence of stellar mass and environment on the size-mass relation. Section 4 presents our discussions about the dependence of the size-mass relation upon environment and redshift. Summary and conclusion are presented in Section 5. Throughout our paper, we adopt the following cosmological parameters: $\Omega_{\rm m} = 0.30$, $\Omega_\Lambda = 0.70$, and $H_0 = 70$ km s^{-1} Mpc^{-1}

2. DATA AND SAMPLE SELECTION

2.1. *Data Description*

The ninth public data release (DR9) of the Legacy Imaging Surveys of DESI covers about 20,000 square degrees in both the South and North Galactic Caps, which provides imaging in $g/r/z$ bands with 5σ depth of 24.7/23.9/23.0 (e.g., Dey et al. 2019; Zou et al. 2022). It consists of three independent optical surveys using three different telescopes: the Beijing-Arizona Sky Survey (BASS; Zou et al. 2017), Mayall z-band Legacy Survey (MzLS), and DECam Legacy Survey (DECaLS). In addition, the imaging surveys provide near-infrared photometric data in the 3.4 and 4.6 μm WISE bands (i.e., Wide-field Infrared Survey Explorer $W1$ and $W2$, see Wright et al. 2010). This data release also includes the 6-year imaging of WISE, with 5σ depths of 20.7 and 20.0 in $W1$ and $W2$ bands, respectively.

Zou et al. (2022) expand their prior research on photometric redshift and cluster detection to the DR9 of DESI Legacy Imaging Surveys, generating a sample of galaxy clusters over 540,000 in the redshift range of $0 < z < 1$. We start from the magnitude-limited sample to identify the galaxy clusters in Section 2.3, using the following criteria listed in Zou et al. (2022) on the DR9 of the legacy imaging surveys:

1. $r < 23$ (the upper limit of r-band magnitude for excluding faint sources).

2. type != "PSF" (the "PSF" refers to point source).

3. fracmasked_$[g, r, z] < 0.5$ (clean photometric cuts using the profile-weighted fraction of pixels masked).

4. fracflux_$[g, r, z] < 0.5$ (clean photometric cuts using the profile-weighted fraction of the flux).

5. fracin_$[g, r, z] > 0.3$ (clean photometric cuts using the fraction of a source's flux within the blob).

6. it is detected in the five bands ($g, r, z, W1, W2$).

7. the photo-z error is set to less than $0.1 \times (1 + z_{\rm phot})$.

8. the range of the r-band absolute magnitude is $-25 < M_r < -16$.

9. the stellar mass range is $10^6 < M_*/M_\odot < 10^{13}$.

10. the uncertainty of logarithmic stellar mass $|\Delta \log(M_*/M_\odot)| < 0.4$ dex.

The photometric redshifts, stellar masses, colors and star formation rates (SFRs) are taken from the catalogue of Zou et al. (2019), which is updated to the DESI DR9 release (Zou et al. 2022).

Using a hybrid technique to estimate photometric redshift ($z_{\rm photo}$), a local linear regression algorithm is applied to a dedicated spectroscopic training set, and then a spectrum template is expertly fitted to determine k-corrections and absolute magnitudes (Beck et al. 2016; Gao et al. 2018). The stellar mass (M_*) and SFR are derived by fitting the photometric spectral energy distribution (SED) of galaxies using the LePhare software [1] (Arnouts et al. 2002; Ilbert et al. 2006). The default Bruzual & Charlot (2003) (BC03) spectral models are employed, in conjunction with the initial mass function (IMF) from Chabrier (2003). Three metallicities (0.004, 0.008, and 0.02) and an exponentially declining star formation history (SFH) from 0.1 to 30 Gyr are taken. For more detailed photometric redshift and stellar mass information please refer to Zou et al. (2019).

Throughout the paper, the size of galaxy is determined by the half-light radius ($R_{\rm e}$) of galaxy model with *the Tractor*. *The Tractor* (Lang et al. 2016) performs profile-fitting photometry. By assuming the same model across all the bands, model fits are determined using only the optical $g/r/z$ data with the specific point spread function (PSF). Four types of the galaxy profiles are used in the fitting procedure of DR9: round

---

[1] https://www.cfht.hawaii.edu/œarnouts/LEPHARE/lephare.html

exponential galaxies with a variable radius ("REX"), de Vaucouleurs ("DEV") profiles (elliptical galaxies), exponential ("EXP") profiles (spiral galaxies), and Sérsic ("SER") profiles. The best-fit model is determined by convolving each model with the specific PSF for each band and minimizing the residuals.

2.2. *Galaxy Clusters*

Previously, Gao et al. (2020) developed a rapid clustering algorithm called Clustering by Fast Search and Find of Density Peaks (CFSFDP) to identify galaxy clusters and their members from the photometric redshift catalog. The key aspect of this algorithm lies in providing a simple and efficient approach for cluster identification, which can quickly identify galaxy cluster centers exhibiting higher density compared to their neighboring regions. This approach successfully eliminates the distorting influence of foreground and background galaxies. Using this algorithm on their sample, Zou et al. (2021) identify 540,432 galaxy clusters at $z \lesssim$ 1 from the DESI legacy imaging surveys. As the galaxy closest to the position of density peak is not always the BCG, they identified the r-band brightest galaxy within 0.5 Mpc around the density peak as the BCG.
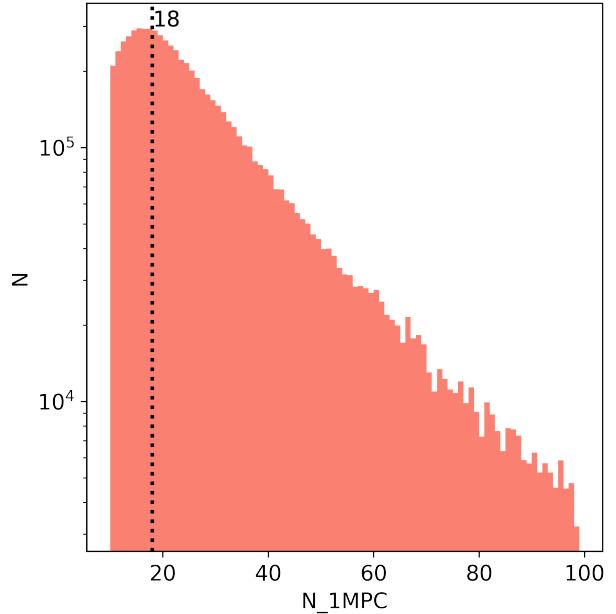
For each galaxy cluster, the number of member galaxies within a distance of 1 Mpc from its center ($N_{1 \text{ Mpc}}$) is used as an estimate of the cluster richness, after correcting for the number of galaxies expected from the background density. Figure 1 displays the histogram distribution of the richness $N_{1 \text{ Mpc}}$ for galaxy clusters. The distribution peaks at around 18, which suggests that galaxy clusters with $N_{1 \text{ Mpc}} > 18$ can be considered as rich clusters with high completeness.

The catalogs of photometric redshifts and clusters used in this paper are available through the ScienceDB Web site[2].

2.3. *Sample Selection*

We select three distinct subsamples from the galaxy cluster catalog, representing three different environments. These subsamples include BCGs located in the densest environmental region of the cluster; member galaxies inhabiting regions of environmental density second only to BCGs; and field galaxies isolated within low-density environments. Our approach to constructing these subsamples is elaborated below:

1. We start with the sample from Zou et al. (2022), selecting galaxies at $z < 0.5$. The upper limit of redshift 0.5 is ultimately determined by the fact

Figure 1. Illustrated in the figure is the distribution of galaxy cluster richness, where $N_{1 \text{ Mpc}}$ signifies the richness of the cluster. The vertical black dashed line denotes the peak of the distribution at ~ 18.

that the corresponding physical size for a typical point spread function in the r-band images ($\sim 0.''8$) is about 5 kpc at $z = 0.5$. If spectroscopic redshift (z_{spec}) is available, we use it preferentially; Otherwise, photometric redshift would be used.

2. To form a subsample of field galaxies, we removed all cluster galaxies, including both BCGs and member galaxies.

3. Taking into account the completeness of galaxy cluster, clusters with a richness greater than 18 (i.e., $N_{1 \text{ Mpc}} ¿ 18$) are selected. Once the clusters are selected, we extract the corresponding BCGs and member galaxies to construct the subsamples of BCGs and member galaxies. To reduce the degree of contamination in membership, we select the galaxies within a projected distance of 0.5 Mpc from the BCGs as member galaxies.

To further investigate the size-mass relation in various types of galaxies, we categorize the galaxies into two types: QGs and SFGs. Numerous studies have shown that QGs and SFGs represent two distinct stages of galaxy evolution, as evidenced by the bivariate distribution in color space (e.g., Baldry et al. 2004; Schawinski et al. 2014). SFGs are a type of galaxies with relatively high SFRs and active star-forming activities. On the

other hand, QGs have entered a phase of inactivity with the cessation of star formation, exhibiting lower SFRs. As reported by Salim (2014) and Bait et al. (2017), there is a remarkable correlation between morphology and specific star formation rate (sSFR = SFR/M_*).

It is essential to provide a combined approach that can distinguish between QGs and SFGs more effectively. As early as the work by Weinmann et al. (2010), researchers select "passive galaxies" using the criterion $\log \mathrm{sSFR} < -11$. Subsequently, an increasing number of studies adopt the criterion of $\log \mathrm{sSFR} = -11$ to differentiate between these two galaxy populations (e.g., Salim et al. 2018; Karunakaran et al. 2023). However, considering the uncertainties in determining stellar mass and SFR, the selection alone by sSFR criterion may not be sufficient. As shown in Figure 2, many SFGs selected by $-11 < \log \mathrm{sSFR} < -7$ appear to be red. Leveraging the advantage of the large sample size provided by the DESI Legacy Imaging Surveys, we can employ more stringent criteria to select QGs and SFGs more reliably. The study conducted by Ilbert et al. (2013) reveals that, at low-redshift ($z < 1$), the independent selection of QGs using the criteria of sSFR ($\log \mathrm{sSFR} < -11$) or color demonstrates a high level of concordance. In practice, we use both sSFR and color as selection criteria to categorize galaxy populations. As a result, after applying the color criterion described below, about 22% red galaxies are found to have $-11 < \log \mathrm{sSFR} < -7$, and about 7.6% blue galaxies have $-15 < \log \mathrm{sSFR} < -11$.

Specifically, we have employed five criteria, as listed below:

1. The r-band magnitude less than 22 to ensure the quantity of photometric redshift (see appendix A).

2. Considering the reliability of the half-light radius measurement, the galaxies with $R_\mathrm{e}/\sigma_{R_\mathrm{e}} > 5$ are selected.

3. A more rigorous criterion than parent catalog is applied to the photometric redshifts, $\sigma_{z_\mathrm{photo}} < 0.05 \times (1 + z_\mathrm{photo})$, to exclude the galaxies with poor SED fittings or inaccurate redshift estimates.

4. The specific star formation rate (sSFR) is utilized to distinguish between quiescent and star-forming galaxies, with the former having $-15 < \log \mathrm{sSFR} < -11$ and the latter with of $-11 < \log \mathrm{sSFR} < -7$.

5. The color criterion is further taken to distinguish the SFGs and QGs. Based on the BC03 templates, the color cut of $(g - z)$ as a function of redshift can be established by tracing the galaxy

template with an exponentially declining SFH ($t = 5$ Gyr; $\mathrm{Z}_\odot$; $\tau < 2$ Gyr). We select red and blue galaxies from the quiescent and star-forming populations, respectively, and form a final sample consisting of both types in three distinct environments. Figure 2 visually illustrates the process of sample selection.

Table 1. Sample size statistics for different environments

Type	Field	Member	BCGs	Sum
QGs	6,844,819	461,636	29,827	7,336,282
(percentage)	(21.36%)	(1.44%)	(0.10%)	(22.90%)
SFGs	24,335,569	363,014	4,495	24,703,078
(percentage)	(75.96%)	(1.13%)	(0.01%)	(77,10%)
Sum	31,180,388	824,650	34,322	32,039,360
(percentage)	(97.32%)	(2.57%)	(0.11%)	(100%)
Total	32,039,360			/
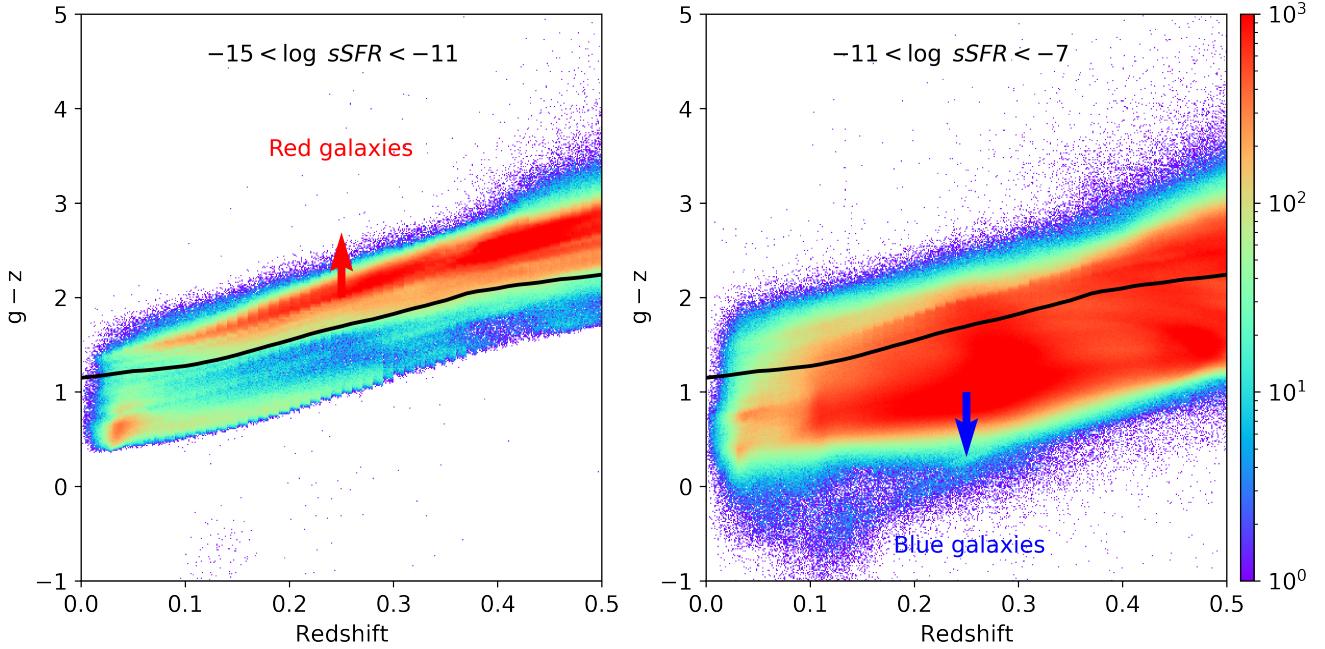
NOTE—The categories "Field, Member, BCGs, QGs, SFGs" correspond to field galaxies, member galaxies, the brightest cluster galaxies, quiescent galaxies, and star-forming galaxies, respectively. The percentages indicate the fraction of different types of subsamples to the total sample.

Table 2. The statistics of BCGs in different redshift bins

Redshift	$0-0.1$	$0.1-0.2$	$0.2-0.3$	$0.3-0.4$	$0.4-0.5$
$\mathrm{N_{QG}}$	601	4,626	8,510	7,372	8,718
percentage	2.01%	15.51%	28.53%	24.72%	29.23%
$\mathrm{N_{SFG}}$	100	352	946	1,002	2,095
percentage	2.22%	7.83%	21.05%	22.29%	46.61%
$\mathrm{N_{ALL}}$	701	4,978	9,456	8,374	10,813
percentage	2.05%	14.50%	27.55%	24.40%	31.50%
$\Sigma(\mathrm{N_{QG}})$	29,827 (86.90%)		$\Sigma(\mathrm{N_{SFG}})$	4,495 (13.10%)	

NOTE—"$\mathrm{N_{QG}}$" represents the number of quiescent galaxies in the redshift bin, while "$\mathrm{N_{SFG}}$" represents the number of star-forming galaxies and "$\mathrm{N_{ALL}}$" represents the total number of galaxies. "$\Sigma(\mathrm{N_{QG}})$" and "$\Sigma(\mathrm{N_{SFG}})$" represents the total number of quiescent and star-forming galaxies without bin distinction, respectively.

Our final total sample comprises 32,039,360 galaxies with $r < 22$ at $z < 0.5$. These galaxies are classified into two types: QGs and SFGs, and have been categorized into three different environments: field galaxies, member galaxies, and BCGs. Statistics on the number of subsamples under different conditions are shown in Table 1, in which field galaxies occupy the majority. Addition-

Figure 2. Rest-frame color-redshift diagram for galaxies with redshifts in the range of $0 < z < 0.5$. The solid black line represents the BC03 template with $\tau = 2$ Gyr. Left panel: Distribution of the sample of quiescent galaxies, which are selected using the sSFR criterion (-15 ¡ log sSFR ¡ -11). Galaxies above the solid black line are classified as QGs. Right panel: Distribution of the sample of star-forming galaxies, which are selected using the sSFR criterion (-11 ¡ log sSFR ¡ -7). Galaxies below the solid black line are classified as SFGs. The color bar represents the number of galaxies.

Table 3. The complete mass at different magnitude limits in different redshift bins

Redshift	Type	r_{lim}	N	$\log(M_{*,\mathrm{comp}}/M_\odot)$
$0 - 0.1$	QGs	18.4	83,136	10.12
$0.1 - 0.2$	QGs	19.7	508,080	10.32
$0.2 - 0.3$	QGs	20.5	1,194,350	10.41
$0.3 - 0.4$	QGs	21.4	1,652,403	10.29
$0.4 - 0.5$	QGs	22.0	2,340,092	10.28
$0 - 0.1$	SFGs	22.0	809,587	8.10
$0.1 - 0.2$	SFGs	22.0	3,705,206	8.79
$0.2 - 0.3$	SFGs	22.0	7,414,001	9.21
$0.3 - 0.4$	SFGs	22.0	4,391,249	9.54
$0.4 - 0.5$	SFGs	22.0	3,564,723	9.85
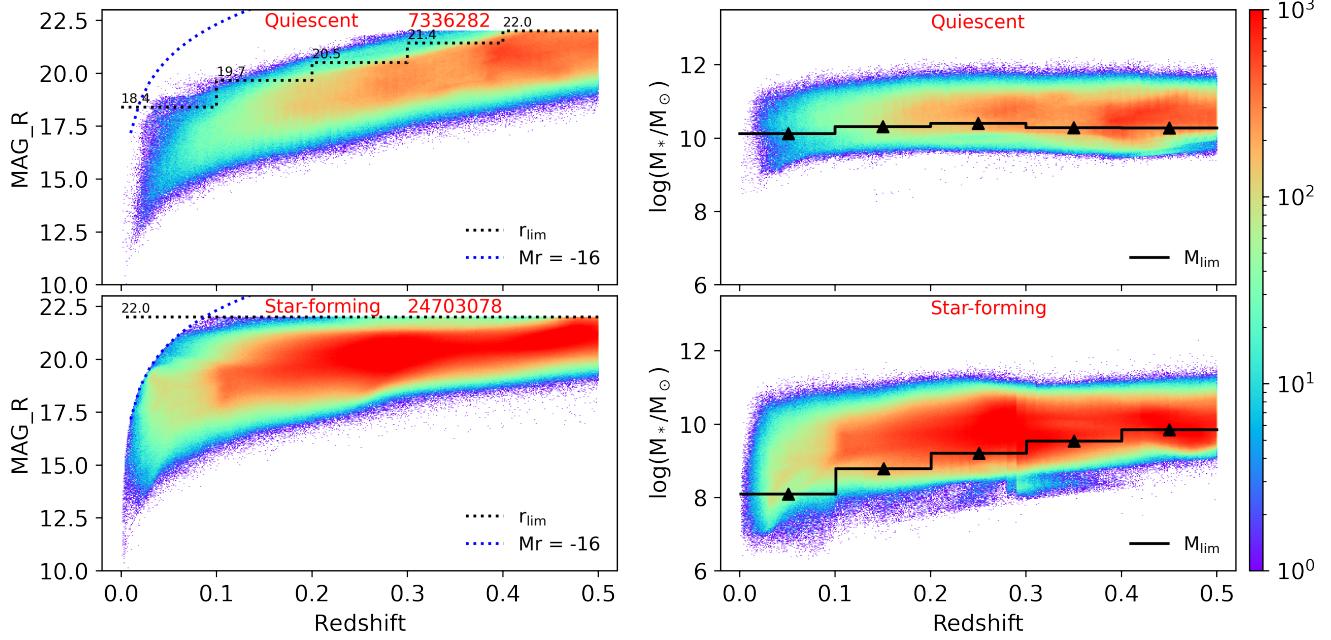
NOTE—"r_{lim}" represents r-band magnitude; "N" represents the number of galaxies that are greater than the mass-complete limit in correspondind redshift interval ($\triangle\ z$ = 0.1); "$\log(M_{*,\mathrm{comp}}/M_\odot)$" represents the mass-complete limit adopted for the corresponding redshift bin.

ally, we provide a count distribution of BCGs, showing that star-forming galaxies constitute a very small fraction (about 13.10%), as demonstrated in Table 2.
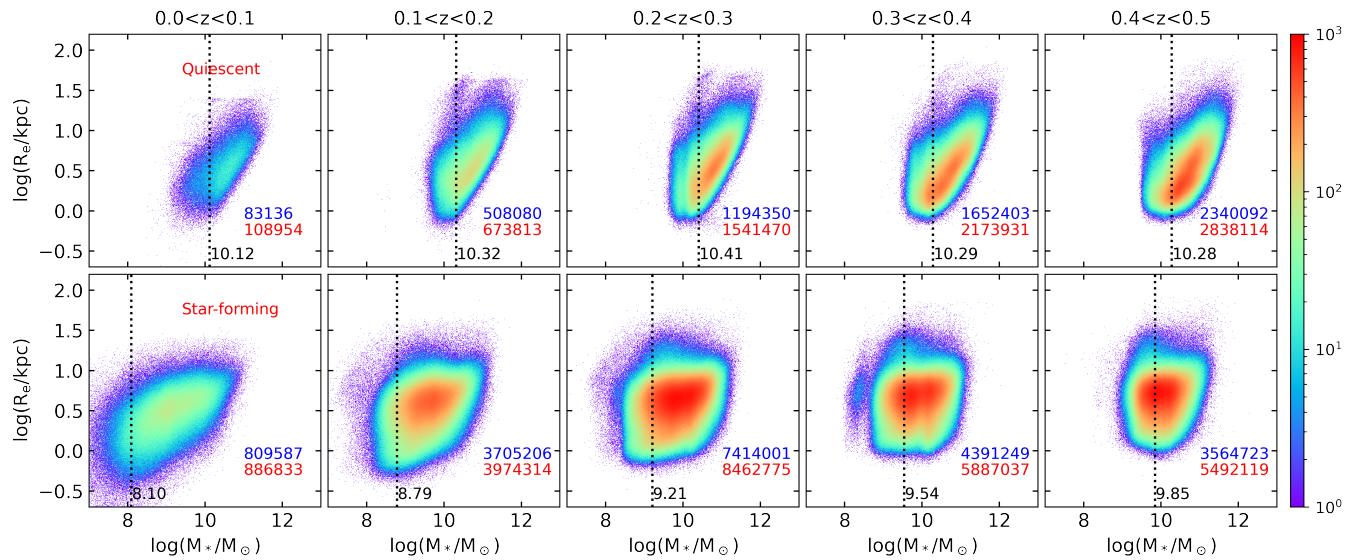
The 90% completeness limit of stellar mass (mass-complete: M_{comp}) is estimated using a method similar to Pozzetti et al. (2010) and Gu et al. (2021). The completeness of stellar mass is affected by both the red-

shift and mass-to-light ratio (M/L ratio) for each galaxy. Given the well-established fact that quiescent galaxies usually have a higher M/L ratio compared to star-forming galaxies, the completeness limits for different galaxy types can vary at different redshifts. We calculate the value of M_{comp} for each redshift bin by determining the stellar mass limit (M_{lim}) for the 20% faintest galaxies within a given redshift bin ($\triangle z = 0.1$), by applying the following formula: $\log M_{\mathrm{lim}} = \log M_* + 0.4 \times (r - r_{\mathrm{lim}})$, where r_{lim} is set as the magnitude limit of our subsamples. For SFGs we use a fixed value of 22.0 as the magnitude limit for each redshift bin. For QGs, based on the distribution of magnitudes at $z < 0.4$, we pick up the r-band magnitude than which 95% galaxies are brighter at each redshift bin as the limiting magnitude (r_{lim}). As a result, the r_{lim} for the five redshift bins are determined to be 18.4, 19.7, 20.5, 21.4, and 22.0, respectively. Subsequently, the final M_{comp} is defined as the upper envelope of M_{lim} distribution below which lie 90% of the M_{lim} values at a given redshift bin.

Figure 3 depicts the distribution of r-band magnitude and stellar mass as a function of redshift. The imposed limit on the r-band absolute magnitude ($M_r < -16$) leads to a dearth of galaxies at the faint end at lower redshifts, as evident from the left panels. However, quiescent galaxies show a different pattern of deficiency com-

Figure 3. Left: Upper and lower panels display the distribution of r-band magnitudes as a function of redshift. Different colors represent different distribution densities of galaxies. Red numbers indicate the total number of galaxies in the subsample. The black dotted lines with black numbers represent the apparent magnitude limit values (r_{lim}) in the corresponding redshift bins, while the blue dotted lines display the r-band absolute magnitude equal to -16 without considering the k-correction. The top panel displays the distribution of QGs with r_{lim} sequentially used as (18.4, 19.7, 20.5, 21.4, 22.0), and the bottom panel illustrates the distribution of SFGs, for which we adopt a fixed r_{lim} value of 22.0 in all redshift bins. The rationale for using different methods to determine the magnitude limits is detailed in section 2.3. Right: Upper and lower panels present the distribution of stellar masses as a function of redshift. The black solid lines in the panel denote the corresponding completeness of stellar mass (M_{comp}) in different bins, while the black triangle indicates the median redshift in each bin.

Figure 4. Size-mass distribution map ($R_e - M_*$) of the total sample. The distribution of R_e and M_* is shown in logarithmic space. The top five panels show the distribution of QGs in five different redshift bins, while the bottom five panels show the distribution of SFGs. The color gradients in the figure indicate the density of galaxies, and the blue/red number in the lower right corner indicates the number of galaxies with mass-complete/total galaxies in that particular redshift bin. The black dotted lines represent the 90% mass-complete limits.

pared to star-forming galaxies, with a more pronounced lack of the former at the faint end. After reviewing our sample and selection criteria, we recognize that some fainter galaxies are excluded due to our implementation of more strict criteria on both colors and sSFRs. Only the quiescent galaxies with red colors are included. In addition, the lack of faint quiescent galaxies at lower redshift may be also related with observational constraints and data processing methods.

Due to this, we adopt the dynamic limits of apparent magnitude to estimate the completeness of stellar mass. The statistics of stellar mass limit and galaxy number in this sample are shown in Table 3, in which a brighter limit of apparent magnitude is settled at lower redshift. Figure 3 also illustrates the adopted limit of apparent magnitude in the left panels and the resulting mass-complete limit in the right panels.

Figure 4 shows the distribution of R_e and M_* in logarithmic space. The total sample is divided into quiescent and star-forming galaxies in five redshift bins ($\triangle z = 0.1$). The black dotted lines show the 90% mass-complete limit. In each redshift bin, we use blue numbers to indicate the quantity of mass-complete subsamples and red numbers to indicate the total number of samples within that bin.

3. SIZE-MASS RELATION

As an important perspective of size-mass relation, mass growth has been discussed by many works. For example, both Schawinski et al. (2014) and Webb et al. (2015) have shown that in the early phase of the galaxy evolution the dominant factor of mass growth is the continuous star formation, and mergers dominate mass growth in the later phase. The evolution of stellar mass directly affects size growth, which has also been demonstrated by many observations (e.g., Lin et al. 2013; Huertas-Company et al. 2013b). For instance, van Dokkum et al. (2010) demonstrate that during the redshift range of $1.4 < z < 2$, the size growth is primarily driven by star formation. For massive galaxies, particularly quiescent galaxies or BCGs, they exhibit a higher slope α in the size-mass relation, indicating that mergers have replaced star formation as the dominant factor in their mass growth (e.g., Naab et al. 2009).

However, the influence of environment on the size-mass relation has not been revealed. Cooper et al. (2012) find a strong relationship between galaxy size and environment for the quiescent galaxies at $1 < z < 2$. And some studies suggest that the environment plays an important role in massive early-type galaxies at the low redshift end (e.g., Yoon et al. 2017). But, Kelkar et al. (2015) compare the mass–size relations of cluster

and field galaxies in the redshift range of $0.4 < z < 0.8$ and finds no significant environmental difference in it. So, how does environment play a role on size growth? Next, the impact of stellar mass and environment on the size-mass relation will be discussed in 3.1 and 3.2, respectively.

3.1. The Effect of Stellar Mass

To examine the correlation between the sizes and masses of quiescent and star-forming galaxies across various redshift bins, three subsamples with distinct environmental densities are utilized. We employ a robust linear model with HuberRegressor (Pedregosa et al. 2011) to fit the correlation, and Figure 5 displays the results. Huber loss functions possess the advantage of being less susceptible to the influence of outliers, while still taking into account their effects to a certain degree. If the absolute error of the sample is less than a certain threshold, the sample will be classified as an internal sample. We set this threshold "epsilon" to 1.35 to achieve 95% statistical efficiency.

The top five panels display the distributions of QGs in five different redshift bins, while the bottom five panels show the distributions of SFGs. The distributions of field galaxies, member galaxies, and BCGs are represented by gradients of blue, green, and red colors, respectively. The number of galaxies in each environment is denoted by numbers of different colors, with the total number of galaxies in the bin highlighted in black, and the slopes are annotated in the lower right corner with the corresponding colors. The best-fitting slopes for the QGs and SFGs in different redshift bins are presented in Table 4.

The size-mass relations for QGs and SFGs within various environments are $R_e \propto M_*^{0.31\sim0.52}$ and $R_e \propto M_*^{0.08\sim0.22}$, respectively. Our results confirms the consistency of the size-mass relations with previous findings in the redshift range of $z < 0.5$ (e.g., Shen et al. 2003; van der Wel et al. 2014; Kawinwanichakij et al. 2021). Furthermore, we compare the slopes among the galaxies in different environments, and find that the slopes of field and member galaxies are similar. This suggests that these galaxies may have undergone similar evolutionary paths, or at least, that the denser environment does not significantly affect the size-mass relations of member galaxies. However, when comparing the slopes of field and member galaxies with those of BCGs, a noticeable steeper slope in the size-mass relation can be seen for BCGs at $z > 0.1$, regardless of star formation status, indicating a potential environmental dependence. To address this complicated phenomenon, we need to consider the mass-complete limit of the sample

in order to remove the potential bias caused by mass incompleteness.

Considering the completeness of stellar mass, we fit the size-mass relations with the galaxies above the mass-complete limits listed in Table 3. Figure 6 presents the results of our analysis with the subsample above mass-complete limits. The best-fitting slopes of size-mass relations for all subsamples are given in Table 4. Compared with Figure 5, field and member QGs have steeper size-mass relations, which leads to slighter difference in slope for the QGs within various environments. The difference in slopes between star-forming BCGs and field/member galaxies at $z > 0.1$ persists noteworthy even with the mass-complete limit subsample.

The slope variations with redshift are shown in Figure 7. To mitigate potential effects stemming from mass incompleteness, we fit the size-mass relation for massive galaxies with $\log(M_*/M_\odot) > 10.41$. Different colored squares represent the slopes of different galaxy types, while error bars denote the mean absolute errors. For quiescent galaxies, we find the highest slope in the redshift bin of $0.2 < z < 0.3$, particularly pronounced for the BCGs. In the case of SFGs, steeper slopes are found at lower redshifts, whereas the slopes are lower at higher redshifts. Our study reveals different trends of redshift evolution of size-mass relation between QGs and SFGs. In general, the slope difference between the QGs and SFGs at $0.1 < z < 0.5$ is significant for various environments, and it tends to be larger at higher redshifts.

However, it remains uncertain what exactly causes the discrepancy in slope between BCGs and field/member galaxies, and it is hard to definitively attribute the difference in size-mass relation to the variations in either mass distribution (namely, subsamples in different environments are composed of galaxies of varying masses) or environmental effect. For eliminating the impact of mass distribution on size-mass relation, we will apply a mass-matching method for unveiling the net effect of environment in Section 3.2.

3.2. *The effect of environment*

Whether the environment affects the size-mass relation is still under debate. At the low redshift end ($z < 0.2$), some studies show that the environment has no influence on the size-mass relation (e.g., Maltby et al. 2010; Huertas-Company et al. 2013a). However, some people hold the opposite view. For example, Yoon et al. (2017) studied the massive early-type galaxies with a redshift range of $0.1 \leqslant z < 0.15$, and believed that the environment has a significant impact on the size-mass
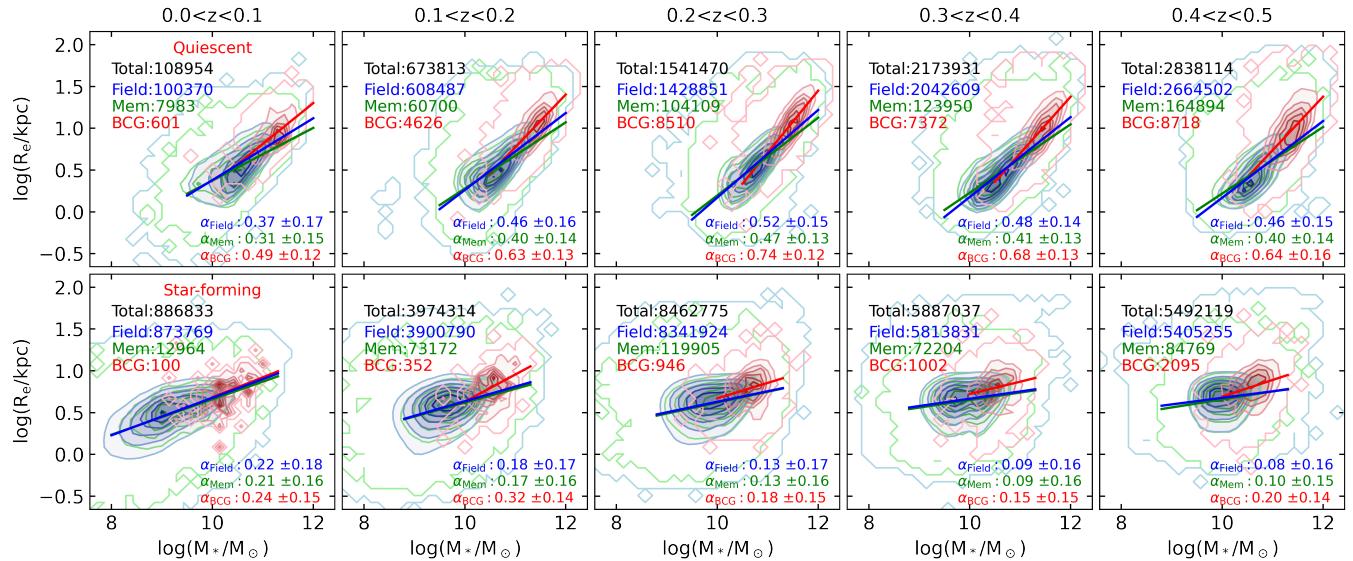
relation when the mass is greater than $10^{11.2} M_\odot$. In addition, at high redshift end, most studies show that the environment is relevant to the size-mass relation (e.g., Lani et al. 2013; Delaye et al. 2014). But all of these studies are based on small samples and different definitions of environment. DESI Legacy Imaging surveys make possible for us to construct large subsamples of QGs and SFGs within different environments (namely, field galaxies, member galaxies of clusters, and BCGs).

In order to eliminate the possible impact of mass and redshift distributions on size-mass relation, we build the mass- and redshift-matched subsamples of BCGs, member galaxies, and field galaxies at $z < 0.5$. Since the number of BCGs is minimum, we try to match the field and member galaxies with similar redshift and mass distributions on the basis of BCG subsample. Following the mass-matching method described in Gu et al. (2019), for each BCG, one matching galaxy is selected from both the field galaxies and member galaxies, respectively. The selected galaxies exhibit the minimum value of $d = \sqrt{(z_i - z_0)^2 + (\log M_{*,i} - \log M_{*,0})^2}$, where $(z_0, M_{*,0})$ represents the position of the given BCG in the redshift-mass space, and $(z_i, M_{*,i})$ represents the location of the galaxies to be matched. For ensuring a robust redshift- and mass-matching, the upper limit of d is set to be 0.04. Each BCG is matched with a similar galaxy in both mass and redshift space. The BCGs that fail to find counterpart galaxies in the above matching process are discarded. As a result, we obtain the mass-matched subsamples of BCGs, field galaxies and member galaxies with similar redshift- and mass-distributions. Finally, three mass-matched subsamples including 26,312 BCGs, 26,312 massive member galaxies, and 26,312 field galaxies are constructed. The Kolmogorov–Smirnov (K-S) tests are performed to check the similarities in mass- and redshift-distributions. Table 5 lists the sample size and the K-S probabilities (P). All of the P-values are much larger than the threshold of 0.05, which ensures the similarities in M_*- and z-distributions for the mass-matched samples.

Figure 8 shows the size-mass relations for the QGs and SFGs in mass-matched subsamples of BCGs, member galaxies and field galaxies. The best-fitting slopes of size-mass relations for mass-matched subsamples are listed in Table 4. Compared with Figure 6, both field and member galaxies have steeper size-mass relations, while quiescent BCGs tend to have flatter size-mass relations. The QGs in fields and clusters show obvious steepening trends in size-mass relations for various redshift bins than the SFGs. In Figure 8, we observed a

Table 4. The slopes α of size-mass relation ($R_e \propto M_*^\alpha$) in different bins
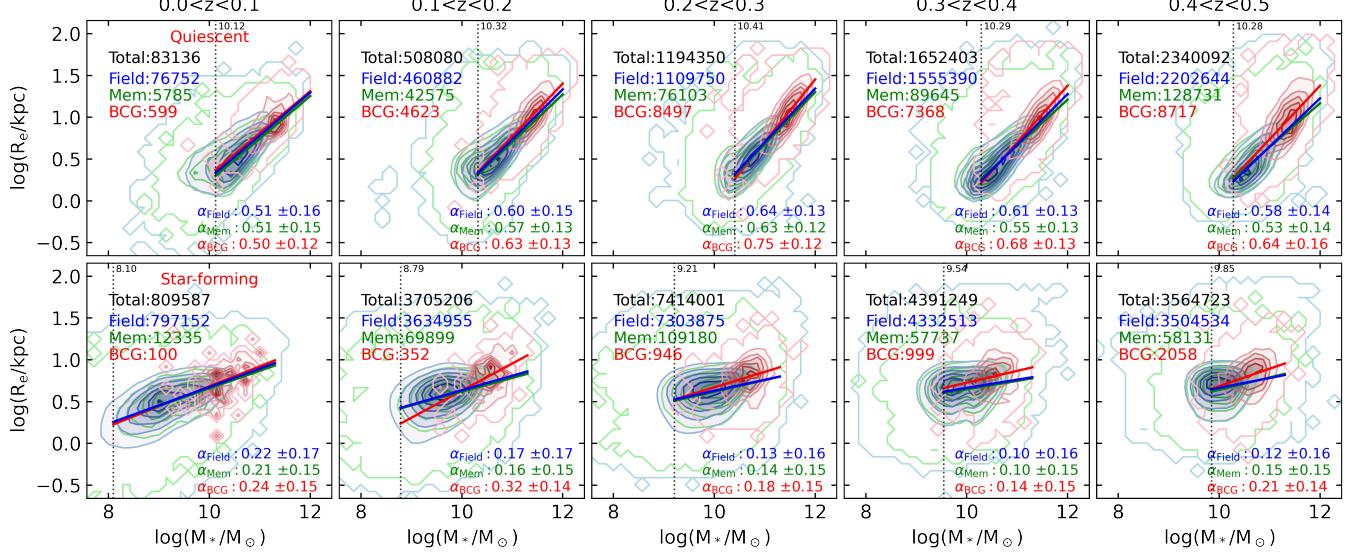
Sample	Environment	Type	z < 0.1	0.1 < z < 0.2	0.2 < z < 0.3	0.3 < z < 0.4	0.4 < z < 0.5
Entire	Field	quiescent	0.37 ± 0.17	0.46 ± 0.16	0.52 ± 0.15	0.48 ± 0.14	0.46 ± 0.15
		star-forming	0.22 ± 0.18	0.18 ± 0.17	0.13 ± 0.17	0.09 ± 0.16	0.08 ± 0.16
	Member	quiescent	0.31 ± 0.15	0.40 ± 0.14	0.47 ± 0.13	0.41 ± 0.13	0.40 ± 0.14
		star-forming	0.21 ± 0.16	0.17 ± 0.16	0.13 ± 0.16	0.09 ± 0.16	0.10 ± 0.15
	BCG	quiescent	0.49 ± 0.12	0.63 ± 0.13	0.74 ± 0.12	0.68 ± 0.13	0.64 ± 0.16
		star-forming	0.24 ± 0.15	0.32 ± 0.14	0.18 ± 0.15	0.15 ± 0.15	0.20 ± 0.14
Mass-complete	Field	quiescent	0.51 ± 0.16	0.60 ± 0.15	0.64 ± 0.13	0.61 ± 0.13	0.58 ± 0.14
		star-forming	0.22 ± 0.17	0.17 ± 0.17	0.13 ± 0.16	0.10 ± 0.16	0.12 ± 0.16
	Member	quiescent	0.51 ± 0.15	0.57 ± 0.13	0.63 ± 0.12	0.55 ± 0.13	0.53 ± 0.14
		star-forming	0.21 ± 0.15	0.16 ± 0.15	0.14 ± 0.15	0.10 ± 0.15	0.15 ± 0.15
	BCG	quiescent	0.50 ± 0.12	0.63 ± 0.13	0.75 ± 0.12	0.68 ± 0.13	0.64 ± 0.16
		star-forming	0.24 ± 0.15	0.32 ± 0.14	0.18 ± 0.15	0.14 ± 0.15	0.21 ± 0.14
Mass-matched	Field	quiescent	0.51 ± 0.13	0.65 ± 0.13	0.69 ± 0.12	0.66 ± 0.12	0.64 ± 0.15
		star-forming	0.27 ± 0.15	0.27 ± 0.14	0.21 ± 0.15	0.18 ± 0.16	0.24 ± 0.15
	Member	quiescent	0.53 ± 0.13	0.67 ± 0.12	0.72 ± 0.11	0.65 ± 0.12	0.64 ± 0.14
		star-forming	0.29 ± 0.13	0.29 ± 0.13	0.23 ± 0.14	0.18 ± 0.15	0.29 ± 0.14
	BCG	quiescent	0.44 ± 0.12	0.58 ± 0.13	0.67 ± 0.12	0.62 ± 0.14	0.61 ± 0.16
		star-forming	0.24 ± 0.15	0.32 ± 0.14	0.18 ± 0.15	0.13 ± 0.15	0.21 ± 0.14
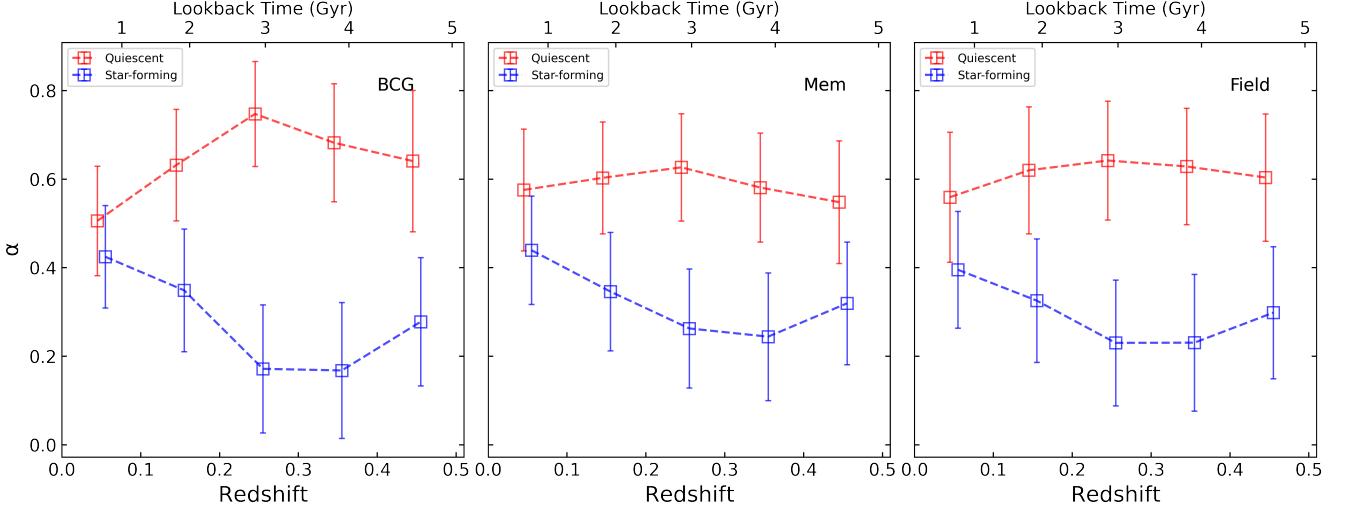
Figure 5. Contour plot of the size-mass distribution. The distribution of R_e and M_* is shown in logarithmic space. The top five panels represent quiescent galaxies in different redshift bins. The contour lines in gradients of blue, green, and red colors depict the distributions of field galaxies, member galaxies, and BCGs, respectively. The legend in the top left corner shows the numbers of galaxies in different subsamples, and the slopes are shown in the lower right corner. The blue, green and red solid lines in the figure represent the least-squares fitting results of field galaxies, member galaxies, and BCGs, respectively. The bottom five panels show the distribution of star-forming galaxies.

clear difference in the intercept of the size-mass relation between the quiescent BCGs and field/member galaxies at $0.4 < z < 0.5$. However, when the uncertainties of slopes are taken into account, the slope differences among the mass-matched subsamples of field galaxies, member galaxies of clusters, and BCGs are negligible for both QGs and SFGs. This suggests that the significant discrepancy in slope between BCGs and field/member

galaxies unveiled in Figure 6 is mainly because BCGs are dominated by massive galaxies covering the high end of mass distribution. After eliminating the effect of mass distribution, environment seems to have little effect on size-mass relations of QGs and SFGs. In other words, mass distribution has been affected by environment, but the ultimate galaxy size is mainly determined by its stellar mass.

Figure 6. Contour plot of the size-mass distribution with a 90% completeness mass limit. The distribution of R_e and M_* is shown in logarithmic space. For the purpose of easy comparison, the contour lines in different colors show the distribution of the total sample. The size-mass relations and legends display the information of the mass-complete subsamples. The black dotted lines in the figure show the mass limit for the 90% completeness sample, and the black number next to the dotted line indicates the corresponding mass-complete limit. The legend in the top left corner shows the numbers of galaxies above the mass limit in different subsamples. This is the main difference from Figure 5.


Figure 7. The slope (α) as a function of redshift (z) is depicted in the figure. The slope of the size-mass relation is fitted by the sample with stellar mass greater than 10.41. We use three panels from left to right to represent the slopes of the subsamples under different environmental densities: BCG, Mem, and Field. The slopes are represented by colored squares, with red indicating quiescent galaxies and blue representing star-forming galaxies; the error bars denote the mean absolute error. Dotted lines connect the slopes across different redshift bins.

The slope variations with redshift for the mass-matched subsamples are shown in Figure 9. Compared with Figure 7, it is confirmed that the mass-matched subsamples of QGs have the highest slope at $0.2 < z < 0.3$, but the trend of SFGs having a higher slope at $z < 0.2$ seems to be alleviated, showing a more consistent slope across different redshift bins. It should
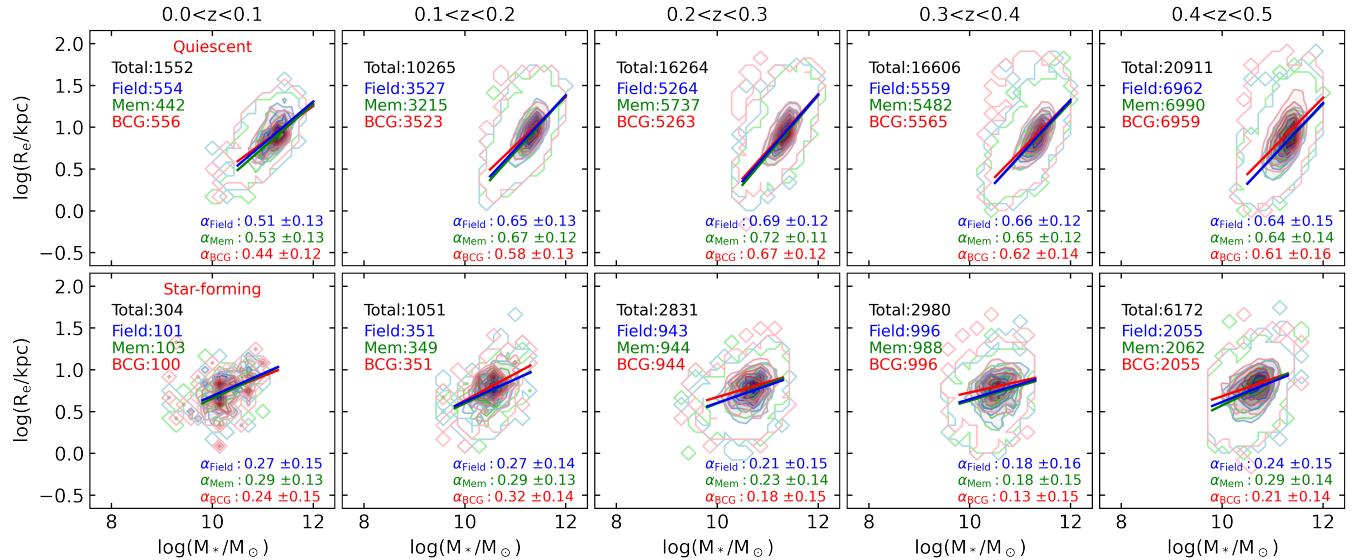
be noted that the trend of slope change with redshift for the QGs and SFGs within three environments is more consistent for the mass-matched subsamples, which further confirms that the size-mass relation is independent upon the environment.

Yoon et al. (2017) found that the early-type galaxies with $M_* > 10^{11.2} M_\odot$ in denser environment tend

Table 5. Subsamples size and the probabilities of K-S tests for the M_*-distributions and z-distributions

Redshift	Galaxy number			M_*-distribution		z-distribution	
Range	BCGs	Member	Field	$P_{\mathrm{M-B}}$	$P_{\mathrm{F-B}}$	$P_{\mathrm{M-B}}$	$P_{\mathrm{F-B}}$
$0 - 0.1$	656	545	655	0.999	0.981	0.810	0.775
$0.1 - 0.2$	3,874	3,564	3,878	0.999	0.982	0.832	0.937
$0.2 - 0.3$	6,207	6,681	6,207	0.786	0.994	0.812	0.944
$0.3 - 0.4$	6,561	6,470	6,555	0.998	0.996	0.998	0.977
$0.4 - 0.5$	9,014	9,052	9,017	0.915	0.992	0.999	0.966

NOTE—"$P_{\mathrm{M-B}}$" represents the P-values of K-S test between member galaxies and BCGs; "$P_{\mathrm{F-B}}$" represents the P-values between field galaxies and BCGs.
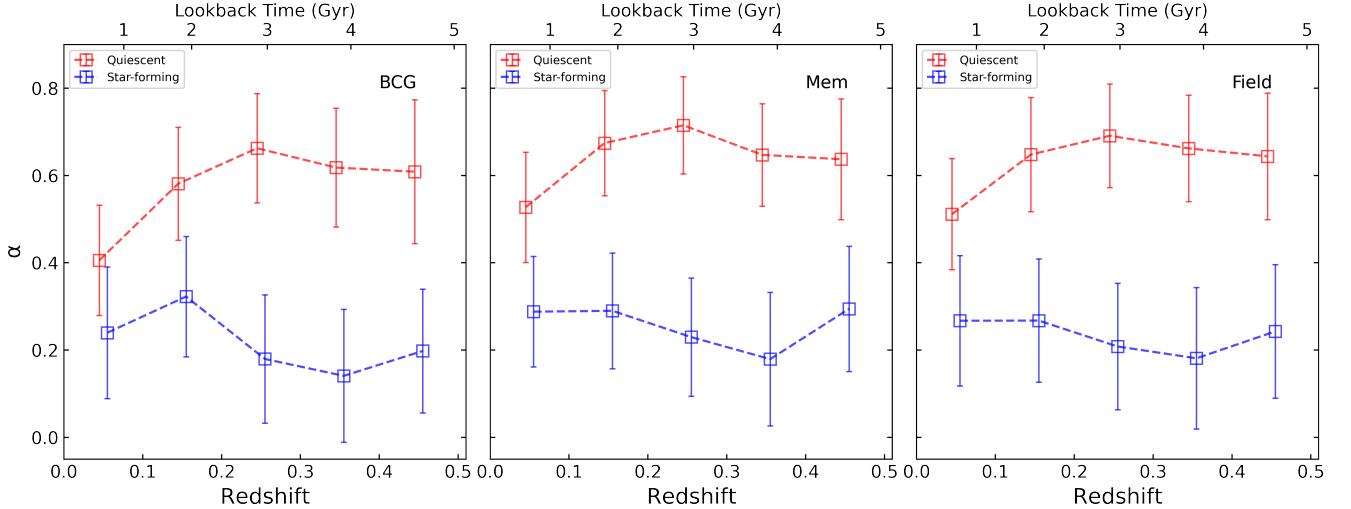
Figure 8. Contour plot of the size-mass distribution with the mass-matched subsamples. The distribution of R_e and M_* is shown in logarithmic space.

to have larger effective radii on the basis of random sampling method, which was attributed to environmental factors. Since the majority of early-type galaxies in high-density regions are quiescent, it is interesting for us to check this tendency via our subsamples of quiescent galaxies. Based on our large mass-matched subsamples of quiescent BCGs, member galaxies, and field galaxies, we achieve different results. It is found that the massive QGs with $M_* > 10^{11.2} M_\odot$ indeed exhibit a higher slope in their mass-size relation with respect to the entire mass-matched QG subsample. However, there is no significant slope difference among the massive BCGs, members, and field galaxies with $M_* > 10^{11.2} M_\odot$. Our finding supports that the steeper slopes in size-mass re-

lation observed in massive galaxies across different environments can be attributed to the difference in the distribution of stellar mass. The environment does not directly influence the size-mass relation, but rather changing the distribution of stellar mass. Stellar mass seems to be the predominant factor for driving the size growth of galaxies.

To sum up, in the star-forming epoch of galaxy evolution (i.e.,SFGs), continuous star formation leads to stellar mass growth. With the increase in stellar mass and gas consumption, star formation activity will halt when its gas supply and reservoir are destroyed. For the quiescent epoch of galaxy evolution, minor mergers become the dominant mode of mass growth in QGs (Bird et al.

Figure 9. The slope (α) as a function of redshift (z) is depicted in the figure. The slope of the size-mass relation is fitted by the mass-matched subsamples. We use three panels from left to right to represent the slopes of the subsamples under different environmental densities: BCG, Mem, and Field. The slopes are represented by colored squares, with red indicating quiescent galaxies and blue representing star-forming galaxies; the error bars denote the mean absolute error. Dotted lines connect the slopes across different redshift bins.

2013; van Dokkum et al. 2015; Naab et al. 2007). This leads to a higher prevalence of massive galaxies for QGs, which is why QGs exhibit a steeper size-mass relation than SFGs (see Figure 6). In general, massive galaxies are more likely to be attracted towards the centers of high-density dark matter halos due to gravitational interactions, which provides more opportunities for galaxy mergers. This makes the high density environment be occupied by more massive galaxies, which is the reason why the most of BCGs are massive QGs. Our work suggests that, for QGs and SFGs, stellar mass is more fundamental factor for size growth, and environments only affect the distribution of stellar mass.

4. DISCUSSION

4.1. *Uncertainties of stellar mass and SFR*

To enhance the robustness of QGs and SFGs classification, we simultaneously employ two criteria: color ($g - z$) and sSFR. The stellar mass and SFR used in this work are derived with the LePhare software by Zou et al. (2019). As described in Carnall et al. (2019), inferring the SFH from the galaxy SED is quite challenging due to the strong evolution of the mass-to-light ratios of stellar populations with age. Generically, the SED-fitting method can recover the stellar mass at an uncertainty of about $0.2 - 0.3$ dex, and even better than 0.2 dex if near-infrared bands are involved (Muzzin et al. 2009; Zou et al. 2019). In our study, the robust photometric redshifts and stellar masses for galaxies are derived from both optical and near-infrared photometry.

There is a high level of consistency in stellar mass found in Zou et al. (2019) when comparing their results with MAGPHYS fitting. In addition, Kaushal et al. (2023) also indicate that, despite the various SFH patterns observed in individual galaxies, the median sSFR is consistent across all mass bins. Nevertheless, it is important to note that sSFR is an exceptionally sensitive indicator in sampling. According to the findings of Leja et al. (2017), the adoption of nonparametric SFHs in Prospector-α, as opposed to the use of parametric SFHs in MAGPHYS, results in an average increase of 0.25 dex in stellar mass and a 0.1 dex decrease in SFR. Therefore, in order to valuate the possible effect due to sSFR inconsistency produced by various SFH treatments, some blue galaxies within $-11 < \log \mathrm{sSFR} < -10.65$ might have been misclassifed as SFGs. Number of these blue galaxies is 400,816, occupying only 1.62% of our star-forming subsample. Consequently, we have strong grounds to dismiss the influence of different fitting models on the outcomes of our research.

4.2. *Size-mass relation fitting and environment effect*

In general, changes in the mass of a galaxy will be accompanied by alterations in its size. Numerous factors impact the transformations in the mass and size of a galaxy, including accretion, activities of star formation, mergers, and environment. We employ the size-mass relation ($R_e \propto M_*^\alpha$), which is a fundamental relation, to explore the size growth of galaxies in relation to stellar mass and environment, further examine the effects of environment on size growth. Shen et al. (2003) apply

a power-law to fit the size-mass relations for early- and late-type galaxies, respectively. A difference in the size-mass relations is found between the low- and high-mass ends of late-type galaxies. It shows a steeper relation $R \propto M_*^{0.4}$ at $M_* > M_0 = 10^{10.6} M_\odot$, and a shallower relation $R \propto M_*^{0.15}$ below M_0. They also find that the relation is significantly steeper for early-type galaxies ($R \propto M_*^{0.55}$). van der Wel et al. (2014) confirm that the size-mass relation obey a single power law for the early- and late-type galaxies over a large redshift range of $0 < z < 3$. A growing body of research suggests that the relationship between size and mass varies across different mass ranges, deviating from a single power law. Mowla et al. (2019) fit the size-mass relation of all types of galaxies (i.e., QGs and SFGs) with a broken power-law up to $z \sim 3$. Analogously, Kawinwanichakij et al. (2021) use a broken power-law to fit the size-mass relation for QGs and SFGs at $z < 1$, respectively. They demonstrate that the size-mass relations of both populations with a clear change of slopes at a pivot stellar mass M_p ($M_p \sim 10^{10.2-10.6} M_\odot$ for QGs, $M_p \sim 10^{10.7} M_\odot$ for SFGs). It may imply that stellar mass is a dominant factor in size growth.

In this paper, we mainly focus on comparing the difference in size-mass relation for the QGs and SFGs at $z < 0.5$ within various environments, and try to observe the fundamental factor driving the change of the slope. The majority of BCGs commonly have higher stellar masses, resulting in the BCG subsample covers a narrower mass range. It is hard to perform a broken power-law to fit the size-mass relations for mass-matched subsamples. Therefore, we adopt single power-law in our fittings.

Using single power-law fitting, the recent work by Afanasiev et al. (2023) studied the size-mass relation for the galaxies in 15 clusters at $1.4 < z < 2.8$ from the CARLA survey. It is found that the size-mass relation does not evolve much from $z \sim 2$ to the present, and their sizes evolve in a similar way for cluster and field galaxies. Moreover, both BCGs and satellite galaxies are found to lie on the same size-mass relation. Similarly, Strazzullo et al. (2023) compare the sizes of field galaxies at $1.4 < z < 1.7$ with the data from massive clusters in the South Pole Telescope Sunyaev Zel'dovich effect survey, and no significant differences in size are revealed between these two different environments. It is interesting that the massive galaxies with $M_* \sim 10^{11} M_\odot$ observed by the James Webb Space Telescope (JWST) in near infrared band appear to be more compact than their rest-frame optical light profiles at cosmic noon on average (Suess et al. 2022). It is worth noting that their studies primarily focus on the galaxies at high redshifts,
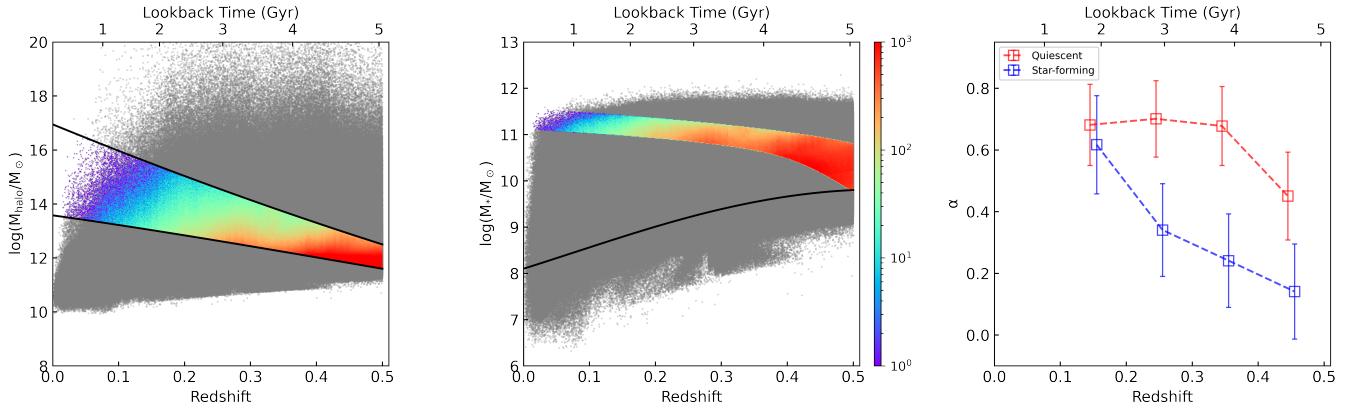
whereas our current work takes use of the galaxies at $z < 0.5$. The environmental effect on the star formation quenching tends to be more significant at $z < 0.5$ (Peng et al. 2010). The large sample of the $z < 0.5$ galaxies from the DESI Legacy Imaging Surveys has great advantages in studying the environment effects on size growth. Our results suggest that stellar mass distribution dominates the size-mass relation, and environmental factors (such as tidal stripping, ram pressure stripping, and harassment) only change their star formation histories. The observed sizes tend to be more closely relative to the accumulated stellar masses, whether they are in field or clusters, and whether they are central or satellite galaxies.

4.3. Redshift evolution of size-mass relation

In Section 3.1 and 3.2, we demonstrate the evolution of the slope for QGs and SFGs in different environments with both mass-complete and mass-matched subsamples, respectively. When considering uncertainties and mass distribution, a similar slope is found for the SFGs in various environments, and a steeper slope is found for the QGs, particularly at $z > 0.1$. Generally, as galaxies transition from SFGs to QGs, the mass growth pattern also undergoes changes, which, in turn, results in alternations in the slope. However, in the context of galaxy evolution, the galaxies with lower masses at higher redshifts should be the progenitors of those at present ($z = 0$). It is interesting to discuss the redshift evolution of the size-mass relation on the basis of the galaxy samples at various redshifts with some possible evolutionary link.

In order to minimize the influence of progenitor bias, we adopt the model of mass accretion histories (MAH), given by McBride et al. (2009) on the basis of dark matter halos from the Millennium simulation, which can be formulated with $M(z) = M_0(1 + z)^\beta e^{-\gamma z}$, where M_0 represents the halo mass at $z = 0$, and β and γ are fitting parameters. By using the MAH model mentioned above, McDonald et al. (2017) took the cluster halo mass at high redshift to track the expected growth trajectory of clusters at lower redshifts. Similarly, we take the halo mass region, $\log M_{\rm halo}/M_\odot \sim 11.6 - 12.5$, as the galaxy-size halos at $z = 0.5$ to trace the corresponding ranges of galaxy halo mass at lower redshifts. Based on the known stellar mass, the corresponding halo mass of a galaxy can be estimated by the stellar-to-halo mass relation (SHMR) that is recently established by Shuntov et al. (2022) with the COSMOS2020 catalog. For the galaxies at $z < 0.5$, the SHMR can be modeled as

$$\log M_{\rm halo} = \log M_1 + \beta \log \frac{M_*}{M_{*,0}} + \frac{(M_*/M_{*,0})^\delta}{1 + (M_*/M_{*,0})^{-\gamma}} - 0.5,$$

Figure 10. Left: the distribution of halo mass and redshift for all the galaxies selected in our work. The colored points denote the galaxies in our growth-tracking subsample; the solid black lines in this panel represent the MAHs for the upper (12.5) and lower (11.6) halo mass limits at $z = 0.5$. Middle: the distribution of stellar mass and redshift for all the galaxies selected in our work. The color bar represents the number of galaxies; the black line represents the mass-complete limit, which is fitted by interpolation. Right: the slope distribution of the size-mass relation for the subsample of growth-tracking galaxies at $0.1 < z < 0.5$. The slopes are represented by colored squares, with red indicating QGs and blue representing SFGs; the error bars denote the mean absolute error.

where all of $\log M_1$, $\log M_{*,0}$, β, δ and γ are the best-fitting parameters given in Shuntov et al. (2022).

The upper and lower limits for halo mass $(\log M_{\mathrm{halo}}/M_\odot)$ at $z = 0.5$ are set to be 11.6 and 12.5 (for a typical galaxy-sized halo), respectively. The stellar mass $(\log M_*/M_\odot)$ corresponding to the lower limit of halo mass is 9.8, which is the lower limit of stellar mass for the mass-complete sample at $0.4 < z < 0.5$. The derived upper limit of stellar mass at $z = 0.5$ is $\log M_*/M_\odot = 10.8$.

As depicted in Figure 10, the left panel illustrates the distribution of halo mass across different redshifts. Colored points represent our growth-tracking subsample, while the solid black lines in this panel represent the MAHs for the upper and lower mass limits. In the middle panel, one can observe the distribution of stellar mass for our subsample, with the color bar indicating the number of galaxies. The right panel displays the distribution of slopes for the growth-tracking subsample. The BCGs have been excluded from this subsample due to their complex evolutionary processes. Due to the limited sample size and larger slope uncertainty at $z < 0.1$, we primarily focus on the slope relation for $0.1 < z < 0.5$. As shown in the right panel, the SFGs exhibit an increase in their slope at lower redshifts, suggesting a change in their size growth pattern. In contrast, QGs demonstrate a relatively stable slope within the range of $0.1 < z < 0.4$, indicating a stable size growth pattern.

We would like to emphasize that the evolutionary link between the galaxies at different redshifts is strongly dependent upon the halo growth model based on the simulations only. Moreover, some QGs at $z = 0$ might have

been evolved from the SFGs at higher redshifts, and the progenitors of some SFGs might be quiescent. For simplicity we neglect the cases that the type of progenitors changes from $z = 0.5$ to 0.1. Therefore, this strategy to create galaxy samples with evolutionarily links should be further validated through a detailed comparison between simulations and observations.

5. CONCLUSION

In this paper we explore the size-mass relations of quiescent and star-forming galaxies in three distinct environments (i.e., BCGs, cluster galaxies, field galaxies), using a large sample of 32,039,360 galaxies with $r < 22$ and $z < 0.5$ selected from the DESI Legacy Imaging Surveys. Based on the color $(g - z)$ and sSFR criteria, these galaxies are divided into QGs and SFGs. The BCGs are found to be dominated by QGs. The difference in size-mass relation for the galaxies within three environments has been investigated, and the main conclusions are the followings:

1. Regardless of galaxy environment, QGs exhibit steeper size-mass relation compared with SFGs, based on both mass-complete and mass-matched subsamples. The slope difference between QGs and SFGs is significant at $0.1 < z < 0.5$ for various environments.

2. The galaxies with greater stellar masses demonstrate steeper size-mass relation. For mass-complete subsamples, BCGs show the highest slope in the size-mass relation when compared to member and field galaxies. No significant difference in slopes is observed between cluster members and field galaxies.

3. The slope variations of the size-mass relation with redshift exhibit distinct characteristics for QGs and SFGs. The slope of QGs reaches its maximum at $0.2 < z < 0.3$, while the slope of SFGs is higher at $z < 0.2$. Compared to the mass-complete subsamples, the mass-matched subsamples exhibit a more consistent trend of slope variation with redshift for the QGs and SFGs within three environments.

4. Based on the mass-matched subsamples of QGs and SFGs, no significant slope difference for the size-mass relation is found among BCGs, cluster members, and field galaxies. It suggests that, though mass growth mode and mass distribution for QGs and SFGs can be affected by galaxy environment, stellar mass is the most fundamental factor driving the size evolution at $z < 0.5$.

APPENDIX

A. THE ACCURACY OF PHOTOMETRIC REDSHIFT

We adopt three parameters to evaluate the quality of photometric redshift at $0 < z < 0.5$ as follows:

1. Bias ($\triangle_{\mathrm{NMAD}}$): the median of systematic deviation between the spectroscopic (z_{spec}) and photometric redshifts (z_{photo}),
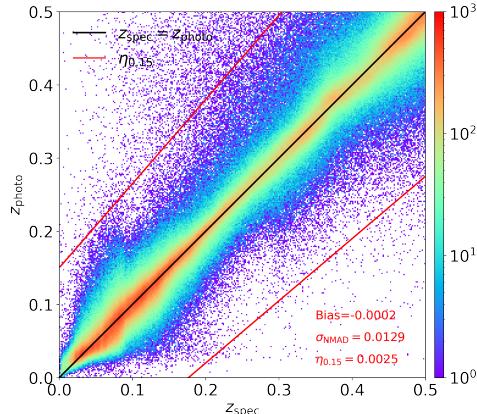
$$\triangle_{\mathrm{NMAD}} = \mathrm{median} \left(\frac{z_{\mathrm{photo}} - z_{\mathrm{spec}}}{1 + z_{\mathrm{spec}}} \right).$$

2. Dispersion ($\sigma_{\triangle_{\mathrm{NMAD}}}$): the dispersion of $\triangle_{\mathrm{NMAD}}$, and the median $\triangle z (= z_{\mathrm{photo}} - z_{\mathrm{spec}})$ is used to calculate normal distribution of median absolute deviation,

$$\sigma_{\triangle_{\mathrm{NMAD}}} = 1.48 \times \mathrm{median} \left(\frac{|\triangle z - \mathrm{median}(\triangle z)|}{1 + z_{\mathrm{spec}}} \right).$$
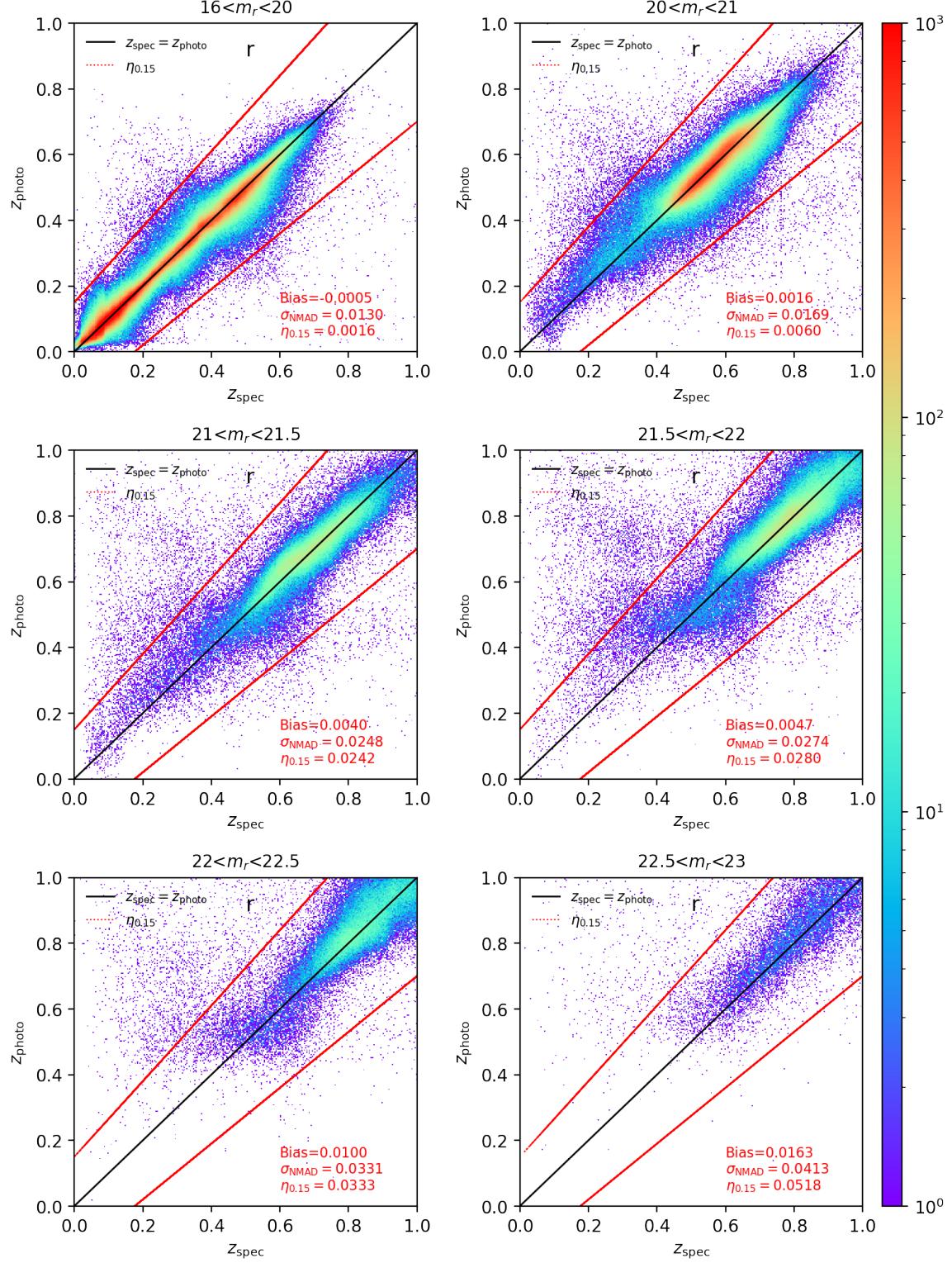
3. Outlier rate ($\eta_{0.15}$): the fraction of galaxies exhibiting significant deviations between their photometric redshifts and spectroscopic redshifts, satisfying

$$\eta = \frac{|z_{\mathrm{photo}} - z_{\mathrm{spec}}|}{1 + z_{\mathrm{spec}}} > 0.15.$$

Figure 11. Photometric redshift (z_{photo}) as a function of spectroscopic redshift (z_{spec}). The color gradients in the figure represent the density of the galaxies. The black solid line in the figure indicates that $z_{\mathrm{spec}} = z_{\mathrm{photo}}$, the red solid lines show the outlier rate of photometric redshifts with $\eta > 0.15$. The value of the three parameters (bias, dispersion and outlier rate) are marked in red at the lower right corner.

The accuracy of photometric redshifts in the range of $z < 0.5$, is $\sigma_{\triangle_{\mathrm{NMAD}}} \approx 0.013$, as shown in Figure 11. Compared with the accuracy about 0.017 for the total sample in Zou et al. (2019), the photometric redshift accuracy is better at $z < 0.5$. To verify the accuracy of photometric redshift as a function of magnitude, we divided the magnitude into six bins, as shown in Figure 12. Three parameters (bias, dispersion and outlier rate) are labelled at the lower right corner of each panel. For the galaxies with $r > 22$, both dispersion and outlier rate exceed 0.03. One possible reason is the lack of spectroscopic data as training sample at the faint end (see also Figure 2 of Zou et al. 2022). The large uncertainty of redshift would enhance the contamination in membership of clusters. To ensure the purity of cluster members, we set the r-band magnitude limit to 22 in further sample selection.

Figure 12. Photometric redshifts v.s. spectroscopic redshifts in six different r-band magnitude bins. The color gradients in the figure represent the density of the galaxies. The black solid line in the figure indicates that $z_{\mathrm{spec}} = z_{\mathrm{photo}}$, the red solid lines show the outlier rate of photometric redshifts with $\eta > 0.15$. The value of the three parameters (bias, dispersion and outlier Rate) are marked in red at the lower right corner.

REFERENCES

Afanasiev, A. V., Mei, S., Fu, H., et al. 2023, A&A, 670, A95, doi: 10.1051/0004-6361/202244634

Arnouts, S., Moscardini, L., Vanzella, E., et al. 2002, MNRAS, 329, 355, doi: 10.1046/j.1365-8711.2002.04988.x

Ascaso, B., Aguerri, J. A. L., Varela, J., et al. 2011, ApJ, 726, 69, doi: 10.1088/0004-637X/726/2/69

Bait, O., Barway, S., & Wadadekar, Y. 2017, MNRAS, 471, 2687, doi: 10.1093/mnras/stx1688

Baldry, I. K., Glazebrook, K., Brinkmann, J., et al. 2004, ApJ, 600, 681, doi: 10.1086/380092

Beck, R., Dobos, L., Budavári, T., Szalay, A. S., & Csabai, I. 2016, MNRAS, 460, 1371, doi: 10.1093/mnras/stw1009

Bekki, K., & Couch, W. J. 2003, ApJL, 596, L13, doi: 10.1086/379054

Bird, J. C., Kazantzidis, S., Weinberg, D. H., et al. 2013, ApJ, 773, 43, doi: 10.1088/0004-637X/773/1/43

Bluck, A. F. L., Conselice, C. J., Buitrago, F., et al. 2012, ApJ, 747, 34, doi: 10.1088/0004-637X/747/1/34

Bruzual, G., & Charlot, S. 2003, MNRAS, 344, 1000, doi: 10.1046/j.1365-8711.2003.06897.x

Bundy, K., Ellis, R. S., Conselice, C. J., et al. 2006, ApJ, 651, 120, doi: 10.1086/507456

Calvi, R., Vulcani, B., Poggianti, B. M., et al. 2018, MNRAS, 481, 3456, doi: 10.1093/mnras/sty2476

Carnall, A. C., Leja, J., Johnson, B. D., et al. 2019, ApJ, 873, 44, doi: 10.3847/1538-4357/ab04a2

Cebrián, M., & Trujillo, I. 2014, MNRAS, 444, 682, doi: 10.1093/mnras/stu1375

Chabrier, G. 2003, PASP, 115, 763, doi: 10.1086/376392

Cooper, M. C., Griffith, R. L., Newman, J. A., et al. 2012, MNRAS, 419, 3018, doi: 10.1111/j.1365-2966.2011.19938.x

De Lucia, G., & Blaizot, J. 2007, MNRAS, 375, 2, doi: 10.1111/j.1365-2966.2006.11287.x

Delaye, L., Huertas-Company, M., Mei, S., et al. 2014, MNRAS, 441, 203, doi: 10.1093/mnras/stu496

Dey, A., Schlegel, D. J., Lang, D., et al. 2019, AJ, 157, 168, doi: 10.3847/1538-3881/ab089d

Dressler, A. 1980, ApJ, 236, 351, doi: 10.1086/157753

Dubinski, J. 1998, ApJ, 502, 141, doi: 10.1086/305901

Gao, J., Zou, H., Zhou, X., & Kong, X. 2018, ApJ, 862, 12, doi: 10.3847/1538-4357/aacbc6

Gao, J., Zou, H., Zhou, X., & Kong, X. 2020, PASP, 132, 024101, doi: 10.1088/1538-3873/ab6151

Greene, J. E., Murphy, J. D., Comerford, J. M., Gebhardt, K., & Adams, J. J. 2012, ApJ, 750, 32, doi: 10.1088/0004-637X/750/1/32

Gu, Y., Fang, G., Yuan, Q., Cai, Z., & Wang, T. 2018, ApJ, 855, 10, doi: 10.3847/1538-4357/aaad0b

Gu, Y., Fang, G., Yuan, Q., et al. 2019, ApJ, 884, 172, doi: 10.3847/1538-4357/ab4512

Gu, Y., Fang, G., Yuan, Q., Lu, S., & Liu, S. 2021, ApJ, 921, 60, doi: 10.3847/1538-4357/ac1ce0

Gunn, J. E., & Gott, J. Richard, I. 1972, ApJ, 176, 1, doi: 10.1086/151605

Huang, K.-H., Fall, S. M., Ferguson, H. C., et al. 2017, ApJ, 838, 6, doi: 10.3847/1538-4357/aa62a6

Huertas-Company, M., Shankar, F., Mei, S., et al. 2013a, ApJ, 779, 29, doi: 10.1088/0004-637X/779/1/29

Huertas-Company, M., Mei, S., Shankar, F., et al. 2013b, MNRAS, 428, 1715, doi: 10.1093/mnras/sts150

Ilbert, O., Arnouts, S., McCracken, H. J., et al. 2006, A&A, 457, 841, doi: 10.1051/0004-6361:20065138

Ilbert, O., Salvato, M., Le Floc'h, E., et al. 2010, ApJ, 709, 644, doi: 10.1088/0004-637X/709/2/644

Ilbert, O., McCracken, H. J., Le Fèvre, O., et al. 2013, A&A, 556, A55, doi: 10.1051/0004-6361/201321100

Jones, C., & Forman, W. 1984, ApJ, 276, 38, doi: 10.1086/161591

Karunakaran, A., Sand, D. J., Jones, M. G., et al. 2023, MNRAS, 524, 5314, doi: 10.1093/mnras/stad2208

Kaushal, Y., Nersesian, A., Bezanson, R., et al. 2023, arXiv e-prints, arXiv:2307.03725, doi: 10.48550/arXiv.2307.03725

Kawinwanichakij, L., Silverman, J. D., Ding, X., et al. 2021, ApJ, 921, 38, doi: 10.3847/1538-4357/ac1f21

Kelkar, K., Aragón-Salamanca, A., Gray, M. E., et al. 2015, MNRAS, 450, 1246, doi: 10.1093/mnras/stv670

Khullar, G., Bayliss, M. B., Gladders, M. D., et al. 2022, ApJ, 934, 177, doi: 10.3847/1538-4357/ac7c0c

Kim, K. J., Bayliss, M. B., Noble, A. G., et al. 2023, ApJ, 955, 32, doi: 10.3847/1538-4357/acecff

Kluge, M., Neureiter, B., Riffeser, A., et al. 2020, ApJS, 247, 43, doi: 10.3847/1538-4365/ab733b

Kravtsov, A. V. 2013, ApJL, 764, L31, doi: 10.1088/2041-8205/764/2/L31

Lani, C., Almaini, O., Hartley, W. G., et al. 2013, MNRAS, 435, 207, doi: 10.1093/mnras/stt1275

Lavoie, S., Willis, J. P., Démoclès, J., et al. 2016, MNRAS, 462, 4141, doi: 10.1093/mnras/stw1906

Leja, J., Johnson, B. D., Conroy, C., van Dokkum, P. G., & Byler, N. 2017, ApJ, 837, 170, doi: 10.3847/1538-4357/aa5ffe

Lidman, C., Suherli, J., Muzzin, A., et al. 2012, MNRAS, 427, 550, doi: 10.1111/j.1365-2966.2012.21984.x

Lidman, C., Iacobuta, G., Bauer, A. E., et al. 2013, MNRAS, 433, 825, doi: 10.1093/mnras/stt777

Lin, Y.-T., Brodwin, M., Gonzalez, A. H., et al. 2013, ApJ, 771, 61, doi: 10.1088/0004-637X/771/1/61

Maltby, D. T., Aragón-Salamanca, A., Gray, M. E., et al. 2010, MNRAS, 402, 282, doi: 10.1111/j.1365-2966.2009.15953.x

McBride, J., Fakhouri, O., & Ma, C.-P. 2009, MNRAS, 398, 1858, doi: 10.1111/j.1365-2966.2009.15329.x

McDonald, M., Allen, S. W., Bayliss, M., et al. 2017, ApJ, 843, 28, doi: 10.3847/1538-4357/aa7740

McLure, R. J., Pearce, H. J., Dunlop, J. S., et al. 2013, MNRAS, 428, 1088, doi: 10.1093/mnras/sts092

Mo, H. J., Mao, S., & White, S. D. M. 1998, MNRAS, 295, 319, doi: 10.1046/j.1365-8711.1998.01227.x

Mowla, L., van der Wel, A., van Dokkum, P., & Miller, T. B. 2019, ApJL, 872, L13, doi: 10.3847/2041-8213/ab0379

Muzzin, A., Marchesini, D., van Dokkum, P. G., et al. 2009, ApJ, 701, 1839, doi: 10.1088/0004-637X/701/2/1839

Naab, T., Johansson, P. H., & Ostriker, J. P. 2009, ApJL, 699, L178, doi: 10.1088/0004-637X/699/2/L178

Naab, T., Johansson, P. H., Ostriker, J. P., & Efstathiou, G. 2007, ApJ, 658, 710, doi: 10.1086/510841

Nersesian, A., Xilouris, E. M., Bianchi, S., et al. 2019, A&A, 624, A80, doi: 10.1051/0004-6361/201935118

Newman, A. B., Ellis, R. S., Bundy, K., & Treu, T. 2012, ApJ, 746, 162, doi: 10.1088/0004-637X/746/2/162

Oemler, Augustus, J. 1974, ApJ, 194, 1, doi: 10.1086/153216

Oliva-Altamirano, P., Brough, S., Lidman, C., et al. 2014, MNRAS, 440, 762, doi: 10.1093/mnras/stu277

Paspaliaris, E. D., Xilouris, E. M., Nersesian, A., et al. 2023, A&A, 669, A11, doi: 10.1051/0004-6361/202244796

Pedregosa, F., Varoquaux, G., Gramfort, A., et al. 2011, Journal of Machine Learning Research, 12, 2825

Peng, Y.-j., Lilly, S. J., Kovač, K., et al. 2010, ApJ, 721, 193, doi: 10.1088/0004-637X/721/1/193

Pichon, C., Pogosyan, D., Kimm, T., et al. 2011, MNRAS, 418, 2493, doi: 10.1111/j.1365-2966.2011.19640.x

Poggianti, B. M., Calvi, R., Bindoni, D., et al. 2013, ApJ, 762, 77, doi: 10.1088/0004-637X/762/2/77

Pozzetti, L., Bolzonella, M., Zucca, E., et al. 2010, A&A, 523, A13, doi: 10.1051/0004-6361/200913020

Salim, S. 2014, Serbian Astronomical Journal, 189, 1, doi: 10.2298/SAJ1489001S

Salim, S., Boquien, M., & Lee, J. C. 2018, ApJ, 859, 11, doi: 10.3847/1538-4357/aabf3c

Saracco, P., Gargiulo, A., Ciocca, F., & Marchesini, D. 2017, A&A, 597, A122, doi: 10.1051/0004-6361/201628866

Schawinski, K., Urry, C. M., Simmons, B. D., et al. 2014, MNRAS, 440, 889, doi: 10.1093/mnras/stu327

Shen, S., Mo, H. J., White, S. D. M., et al. 2003, MNRAS, 343, 978, doi: 10.1046/j.1365-8711.2003.06740.x

Shibuya, T., Ouchi, M., & Harikane, Y. 2015, ApJS, 219, 15, doi: 10.1088/0067-0049/219/2/15

Shuntov, M., McCracken, H. J., Gavazzi, R., et al. 2022, A&A, 664, A61, doi: 10.1051/0004-6361/202243136

Smith, G. P., Kneib, J.-P., Smail, I., et al. 2005, MNRAS, 359, 417, doi: 10.1111/j.1365-2966.2005.08911.x

Strazzullo, V., Pannella, M., Mohr, J. J., et al. 2023, A&A, 669, A131, doi: 10.1051/0004-6361/202245268

Suess, K. A., Bezanson, R., Nelson, E. J., et al. 2022, ApJL, 937, L33, doi: 10.3847/2041-8213/ac8e06

van der Wel, A., Franx, M., van Dokkum, P. G., et al. 2014, ApJ, 788, 28, doi: 10.1088/0004-637X/788/1/28

van Dokkum, P. G., Whitaker, K. E., Brammer, G., et al. 2010, ApJ, 709, 1018, doi: 10.1088/0004-637X/709/2/1018

van Dokkum, P. G., Nelson, E. J., Franx, M., et al. 2015, ApJ, 813, 23, doi: 10.1088/0004-637X/813/1/23

Webb, K. A., Villaume, A., Laine, S., et al. 2022, MNRAS, 516, 3318, doi: 10.1093/mnras/stac2417

Webb, T. M. A., Muzzin, A., Noble, A., et al. 2015, ApJ, 814, 96, doi: 10.1088/0004-637X/814/2/96

Weinmann, S. M., Kauffmann, G., van den Bosch, F. C., et al. 2009, MNRAS, 394, 1213, doi: 10.1111/j.1365-2966.2009.14412.x

Weinmann, S. M., Kauffmann, G., von der Linden, A., & De Lucia, G. 2010, MNRAS, 406, 2249, doi: 10.1111/j.1365-2966.2010.16855.x

Whiley, I. M., Aragón-Salamanca, A., De Lucia, G., et al. 2008, MNRAS, 387, 1253, doi: 10.1111/j.1365-2966.2008.13324.x

White, S. D. M., & Frenk, C. S. 1991, ApJ, 379, 52, doi: 10.1086/170483

White, S. D. M., & Rees, M. J. 1978, MNRAS, 183, 341, doi: 10.1093/mnras/183.3.341

Whitney, A., Conselice, C. J., Bhatawdekar, R., & Duncan, K. 2019, ApJ, 887, 113, doi: 10.3847/1538-4357/ab53d4

Williams, R. J., Quadri, R. F., Franx, M., van Dokkum, P., & Labbé, I. 2009, ApJ, 691, 1879, doi: 10.1088/0004-637X/691/2/1879

Williams, R. J., Quadri, R. F., Franx, M., et al. 2010, ApJ, 713, 738, doi: 10.1088/0004-637X/713/2/738

Wright, E. L., Eisenhardt, P. R. M., Mainzer, A. K., et al. 2010, AJ, 140, 1868, doi: 10.1088/0004-6256/140/6/1868

Yoon, Y., Im, M., & Kim, J.-W. 2017, ApJ, 834, 73, doi: 10.3847/1538-4357/834/1/73

Zou, H., Gao, J., Zhou, X., & Kong, X. 2019, ApJS, 242, 8, doi: 10.3847/1538-4365/ab1847

Zou, H., Zhou, X., Fan, X., et al. 2017, PASP, 129, 064101, doi: 10.1088/1538-3873/aa65ba

Zou, H., Gao, J., Xu, X., et al. 2021, ApJS, 253, 56, doi: 10.3847/1538-4365/abe5b0

Zou, H., Sui, J., Xue, S., et al. 2022, Research in Astronomy and Astrophysics, 22, 065001, doi: 10.1088/1674-4527/ac6416